Nuclear Science and Techniques (2025) 36:11
https://doi.org/10.1007/s41365-024-01565-4

Steady-state and transient investigation of a small pressurized water reactor ACPR50S for different ATFs based on Bamboo-C code

Kun Zhuang[1] · Ying-Zhen Wang[1] · Li-Na Deng[1] · Yong-Zhan Wang[1] · Wen Shang[1] · Si-Peng Wang[1]

Received: 14 November 2023 / Revised: 26 January 2024 / Accepted: 17 March 2024 / Published online: 19 December 2024

Abstract

Small modular reactors have received widespread attention owing to their inherent safety, low investment, and flexibility. Small pressurized water reactors (SPWRs) have become important candidates for SMRs owing to their high technological maturity. Since the Fukushima accident, research on accident-tolerant fuels (ATFs), which are more resistant to serious accidents than conventional fuels, has gradually increased. This study analyzes the neutronics and thermal hydraulics of an SPWR (ACPR50S) for different ATFs, $BeO + UO_2 - SiC$, $BeO + UO_2 -$ FeCrAl, $U_3Si_2 -$ SiC, and $U_3Si_2 -$ FeCrAl, based on a PWR fuel management code, the Bamboo-C deterministic code. In the steady state, the burnup calculations, reactivity coefficients, power and temperature distributions, and control rod reactivity worth were studied. The transients of the control rod ejection accident for the two control rods with the maximum and minimum reactivity worth were analyzed. The results showed that 5% B-10 enrichment in the wet annular burnable absorbers assembly can effectively reduce the initial reactivity and end-of-life reactivity penalty. The $BeO + UO_2 -$ SiC core exhibited superior neutronic characteristics in terms of burnup and negative temperature reactivity compared with the other three cases owing to the strong moderation ability of $BeO + UO_2$ and low neutron absorption of SiC. However, the U_3Si_2 core had a marginally better power-flattening effect than $BeO + UO_2$, and the differential worth of each control rod group was similar between different ATFs. During the transient of a control rod ejection, the changes in the fuel temperature, coolant temperature, and coolant density were similar. The maximum difference was less than 10 °C for the fuel temperature and 2 °C for the coolant temperature.

Keywords ACPR50S · Small pressurized water reactor · ATF · Steady · Transient

1 Introduction

Since the 1990s, small modular reactors (SMRs) have received widespread attention owing to their inherent safety, low investment, and flexibility [1]. Many SMR concepts have been proposed, such as gas-cooled small reactors, liquid metal-cooled small reactors, and small pressurized water reactors (SPWRs) [2–4]. PWRs have been researched for many years owing to their mature technology and low implementation difficulty. Furthermore, the SPWR has become the mainstream design [5–12].

A floating nuclear power station, MH-1A [13], was the first SPWR concept. It was built on a converted liberty ship and was part of a series of reactors in the US Army Nuclear Power Program, which developed small nuclear reactors to generate electrical and space heating energy primarily at remote, relatively inaccessible sites. Westinghouse and the Massachusetts Institute of Technology also proposed the floating nuclear power station concepts [14]. Recently, a 50 MWe small modular reactor Nuscale was certified by the US Nuclear Regulatory Commission [15]. The first floating nuclear power station, Akademik Lomonosov, powered by two KLT-40 S reactors, was constructed in Russia [16]. KLT-40 S produces 150 MW of thermal power (approximately 52 MWe at 35% efficiency) and uses low

This work was supported by the National Natural Science Foundation of China (No. 12205150), Natural Science Foundation of Jiangsu Province (No. BK20210304), China Postdoctoral Science Foundation (Nos. 2020M681594 and 2019TQ0148), and Jiangsu Province Postdoctoral Science Foundation (Nos. 2020Z231).

✉ Kun Zhuang
kzhuang@nuaa.edu.cn

[1] Department of Nuclear Science and Technology, Nanjing University of Aeronautics and Astronautics, Nanjing 211106, China

enriched uranium fuel enriched below 20%, averaging at 14.1% enrichment. The thermal hydraulics, breeding ratio, and depletion of KLT-40 S were studied between 2011 and 2020. Furthermore, new floating nuclear power stations were developed in Russia based on new SPWR concepts such as ABV, SVBR, RITM 200, and VBER [17–19]. Argentina resumed the development of CAREM, an SPWR with an electric power output ranging from 150 MW to 300 MW [20]. Japan proposed a 350 MWth integrated SPWR design [21]. South Korea has developed SMART, a 100 MW SPWR that can provide power and desalinate seawater [8]. China proposed the SPWR concept of ACP100S in 2010 and a floating nuclear power plant ACPR50S with a thermal power of 310 MW in 2015 [10, 22]. Uranium dioxide fuel and zirconium alloy claddings are widely used in current PWR designs. Despite its significant potential, the high fuel central temperature and zirconium–water chemical reaction limit its application in advanced SPWRs. The Fukushima nuclear power plant accident was partly caused by the major shortcomings of the traditional uranium–zirconium fuel system [23]. Some studies on the chemical interaction between uranium-oxide fuel pellets and zirconium alloy cladding, control rod ejection accident simulation, and sensitivity analysis in PWRs have also been performed [24, 25]. Hydrogen generated by the zirconium–water chemical reaction can accumulate at dangerous levels and cause explosions. Therefore, the research and development of new fuels and cladding materials to replace current uranium–zirconium fuel systems are urgently required. Accident-tolerant fuels (ATFs) have been developed globally to improve the safety of nuclear power plants during accidents [26]. Generally, ATFs focus on accident-tolerant fuel pellets by improving their thermal conductivity to decrease the fuel temperature and accident-tolerant cladding materials by reducing the rate of the chemical reaction between water and the cladding. Compared with traditional fuel systems, ATFs can resist serious accidents for a long time. The material characteristics of ATFs can slow down the accident process, allowing more time to take emergency measures and greatly reducing the risk of radioactive product leakage. ATF research contains three roadmaps [23]: (1) improving the zirconium alloy by changing the ratio of trace elements to improve oxidation resistance, (2) using new cladding materials such as FeCrAl, SiC, and molybdenum (Mo) alloys, (3) using new fuels with high thermal conductivity and a strong ability to contain fission products, such as nitride fuels, silicide fuel, and fully ceramic microencapsulated fuel.

Extensive research on the use of ATFs in PWRs has been conducted both locally and globally. In 2013, neutronics, thermal hydraulics, and thermodynamics were analyzed for a traditional PWR with fully ceramic microencapsulated (FCM) pellet fuel [27]. In 2014, Chun et al. studied the cladding peak temperature during small- and large-break loss-of-coolant accidents [28]. In 2016, the neutronic characteristics of AP1000 were studied for different ATFs including the cladding material of SiC, FeCrAl alloy, and Mo alloy [29]. In 2017, the University of Wisconsin-Madison confirmed the good performance of FeCrAl alloy claddings in reducing hydrogen production and delaying accident processes [30]. Sadiel et al. studied the neutronic performance of the NuScale core by using ATFs (U_3Si_2) with different coating materials (Cr and FeCrAl) [31]. Kyung Hee University applied FCM fuel to a SPWR, SMART, and analyzed its thermal–hydraulic characteristics. In 2021, Mohsen et al. analyzed the comparative neutronic and thermal–hydraulic characteristics of nitride fuels (UN), carbide fuel (UC), and UO_2 fuels based on the VVER 1000 fuel assembly [32]. In 2020, the nuclear regulatory commission reviewed ATF and cladding designs to identify the fuel/cladding behavior, degradation, and radiological release [33], including silicide fuels (U_2Si_3), UN, and UC for fuel design, and Cr, FeCrAl, and SiC for cladding design. Research on ATFs has also been conducted in China. In 2014, Harbin Engineering University studied the feasibility of applying ATF FCM pellets to an SPWR and the neutronic characteristics of silicon carbide cladding–ATF combinations in small modular reactors [34–37]. Xi'an Jiaotong University analyzed the transient response of CPR1000 PWR with FCM-SiC in large-break losses of coolant accidents and the variation in cladding temperature for different ATF systems based on RELAP5 code [38]. In 2020, the South China University of Technology conducted a safety analysis for a Nuscale reactor employing U_3Si_2, U_3Si_5, FeCrAl, and SiC [39]. Sun Yat-sen University studied the neutronics of UO_2-BeO fuel with various claddings, including SiC and FeCrAl [40].

As mentioned above, some studies on ATFs in PWRs have been conducted domestically and internationally with a focus on ATF characteristics during accidents especially for UO_2-BeO fuel, U_2Si_3, FeCrAl claddings, and SiC claddings. ACPR50S is a modular marine-pressurized water reactor with a thermal power of 300 MW; it was designed by China general nuclear power to develop a floating nuclear power plant. In this study, the neutronic and thermal–hydraulic characteristics of a SPWR, ACPR50S, with different ATFs were studied using the PWR fuel management code Bamboo-C, which was developed by the Nuclear Engineering Computational Physics Laboratory at Xi'an Jiaotong University (NECP lab) [41]. Four types of ATFs including $BeO + UO_2 - SiC$, $BeO + UO_2 - FeCrAl$, $U_3Si_2 - SiC$, and $U_3Si_2 - FeCrAl$ were employed. Various steady-state analyses were performed, including burnup calculations and the calculation of reactivity coefficients, power and temperature distributions, and control rod reactivity worth. The transients of the control rod ejection accident for the two control rods with the maximum and minimum reactivity worth were analyzed. The remainder of this paper is organized as follows. In

Sect. 2, the ACPR50S reactor core and calculation method are introduced. Steady-state and transient analyses are presented in Sect. 3 and 4, respectively. Finally, the conclusions are summarized in Sect. 5.

2 Reactor configurations and calculation method

The goal of ATF is to develop safer fuel types to replace traditional UO_2 fuel and Zr-4 alloy claddings. This study applied ATF to ACPR50S to improve safety and decrease nuclear power generation costs. Furthermore, steady-state and transient neutronics/thermal–hydraulic characteristics were analyzed using Bamboo-C code, which is based on the "two-step" procedure, coupled neutronic diffusion calculation, and parallel multichannel thermal–hydraulic calculation.

2.1 Accident-tolerant fuel

The primary focus of research on advanced fuel technologies is the selection of appropriate fuels and cladding materials. The main method of improving the thermal conductivity of ATF pellets is to incorporate materials with high thermal conductivity into the matrix including doped high-thermal-conductivity UO_2 pellets (UO_2+ BeO/SiC/Mo), uranium silicon compound pellets (U_3Si_2), FCM pellets, UN, and inert matrix dispersion pellets.

Materials such as BeO, SiC, carbon nanomaterials, and metals are suitable for doping UO_2, owing to their high thermal conductivities. BeO is chemically stable, thermally conductive, compatible with cladding materials, and has a low neutron absorption cross section. Compared with UO_2, the uranium-nitride-based composite fuel has a higher fuel density and better thermal conductivity. However, the high amount of U-238 in UN and the added cost of N-15 enrichment make its economic benefits less noticeable. Moreover, it can easily chemically react with water at high temperatures. Uranium-silicon compounds, U_3Si and U_3Si_2, exhibit excellent thermodynamic properties, making them ideal candidates. When subjected to high temperatures and irradiation, U_3Si_2 exhibits enhanced stability and improved resistance to swelling. With the aim of small-scale improvement in existing SPWRs, ATF is used to improve the thermal conductivity of the fuel. In this study, a uranium dioxide-based ATF, UO_2+ BeO, and U_3Si_2, which has good swelling resistance, was selected.

Claddings under accident conditions are among the most fragile structures of a reactor, and new cladding materials with accident tolerance must be considered. After evaluation, the cladding materials that could replace the Zr-4 alloy mainly included metal and ceramic materials [31–33]. Metallic materials include FeCrAl, Mo, and other refractory metals and their alloys, while ceramic materials include SiC and its composite materials. Mo has a high melting point and thermal conductivity, as well as large neutron absorption cross sections, which can result in large reactivity penalties. The loss of the neutron economy can be compensated by reducing the thickness of the cladding; however, this will increase the technical difficulty and research and development costs. FeCrAl alloys have been widely used owing to their good mechanical properties and high-temperature oxidation resistance. High-temperature steam oxidizes their surfaces, and dense oxides are generated to prevent further oxidation. Similarly, they have the disadvantage of a large reactivity penalty due to neutron absorption. In 2017, the China Nuclear Power Research and Design Institute developed a full-scale FeCrAl alloy cladding tube for the first time and conducted irradiation tests. Given these disadvantages, FeCrAl alloy can be set as a short-term development target for ATF claddings. The SiC composite material not only has high strength but can also maintain its good mechanical properties and radiation resistance under the high-temperature and high-pressure conditions of the reactor. Simultaneously, it maintains good compatibility with UO_2 fuel pellets.

As mentioned above, UO_2+BeO and U_3Si_2 and FeCrAl and SiC were chosen for the fuel and cladding as ACPR50S's candidate materials, respectively. Thus, the neutronic and thermal–hydraulic characteristics of four new fuel cladding systems, BeO + UO_2 – SiC, BeO + UO_2– FeCrAl, U_3Si_2– SiC, and U_3Si_2– FeCrAl, were analyzed based on the PWR fuel management code, Bamboo-C, developed by NECP.

2.2 ACPR50S core description

The core arrangement of the SPWR, ACPR50S, is shown in Fig. 1, which contained 21 burnable poison assemblies and 16 control assemblies, with light water acting as the

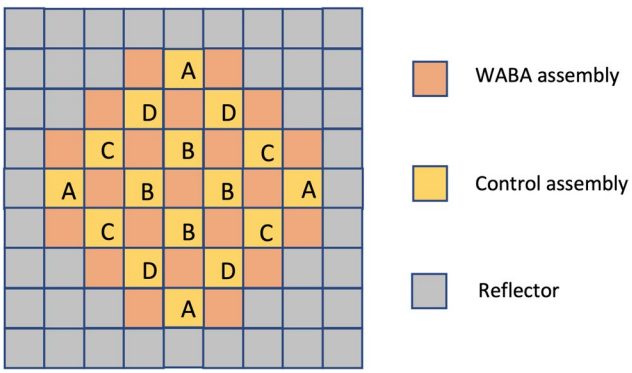

Fig. 1 (Color online) Radial configuration of ACPR50S

surrounding reflector. The thermal power was 300 MW, and the design parameters of the core are listed in Table 1.

Control rods and burnable poisons were employed in ACPR50S to control the reactivity during operation. The control rod is a silver-indium-cadmium alloy (Ag–In–Cd) composed of 80% silver, 15% indium, and 5% cadmium, and the burnable poison adopts wet annular burnable absorbers (WABA) developed by Westinghouse Electric Company. A WABA rodlet comprises annular pellets of an alumina-boron carbide (Al_2O_3/B_4C) burnable absorber material contained within two concentric Zircaloy-4 tubes. Each WABA rodlet contained an annular plenum that accommodated the helium gas released from the reaction between boron and neutrons. As shown in Fig. 2, the assembly was configured using a 17×17 array of fuel, control, and WABA rods. The pitch size of the assembly was 21.41728 cm. The WABA assembly contained 21 WABA rods, and the control assembly contained 33 control rod guide tubes.

2.3 Bamboo-C code

Bamboo-C code was developed in-house by the Nuclear Engineering Computational Physics Laboratory (NECP) at Xi'an Jiaotong University based on "two-step" PWR fuel management [41, 42]. The calculation flowchart for Bamboo-C is shown in Fig. 3, which includes the lattice code LOCUST, core calculation code SPARK, and the lattice core link code LtoS.

LOCUST adopts a multi-group library based on the ENDF/B-VII.0 evaluated library, a global–local method to calculate an effective self-shielding cross section, and a modular MOC method to efficiently solve the neutron transport equation. The point burnup Bateman equation was solved using the high-efficiency CRAM method. The few-group homogenization cross section was calculated using the equivalent homogenization method.

The few-group homogenization parameters under discrete operation states generated by the LOCUST code are functionalized by LtoS code using the least-squares fitting or linear interpolation methods. The few-group homogenization parameters at the target state position can be expressed as the sum of the base state and disturbance terms, as shown in Eq. (1). The functionalization coefficients obtained by fitting or the linear interpolation method are saved in files and used in the following reactor core calculation:

$$\Sigma(S, Bu) = \Sigma_b(S_b, Bu) + \delta\Sigma(S, Bu), \tag{1}$$

where Σ represents the assembly homogenized parameters; Σ_b represents the parameters at the base state; $\delta\Sigma$ is the disturbance term; S is a set of state parameters, including fuel temperature, coolant density, coolant temperature, boron concentration, and control rods; S_b is the state parameter at the base state; and Bu is the burnup level.

For the disturbance term $\delta\Sigma$, LtoS code can optionally use polynomial fitting or a multidimensional Lagrangian interpolation method. In addition, only the multidimensional Lagrangian interpolation method was used for the burnup parameter Bu, as shown in Eq. (2) and Eq. (3):

$$\Sigma_b(S_b, Bu) = c_m\Sigma_b(S_b, Bu_m) + c_n\Sigma_b(S_b, Bu_n), \tag{2}$$

$$\delta\Sigma(S, Bu) = c_x\delta\Sigma_b(S, Bu_x) + c_y\delta\Sigma(S, Bu_y), \tag{3}$$

Table 1 ACPR50S design parameters and ATF parameters

Parameters	Value
Thermal power (MWt)	300
Number of assembly	37
Height of active core (m)	2.5
Assembly pitch (cm)	21.41728
Average power density (MWt/m^3)	49.03
Cladding (wt%)	FeCrAl: Fe/Cr/Al=75/20/5 SiC: Si/C=70.08/29.92
Fuel (wt%)	BeO–UO_2: U/Be/O = 85.806/0.954/13.230 U_3Si_2: U/Si = 92.7237/7.2763
Enrichment of BeO–UO_2 (%)	4.8
BeO volume fraction in BeO–UO_2 (%)	10
UO_2/BeO density (g/cm^3)	10.47/2.85
U_3Si_2 density (g/cm^3)	11.57
Zr-4 density (g/cm^3)	6.56
FeCrAl density (g/cm^3)	7.1
SiC density (g/cm^3)	2.58
Radius of fuel pellet (mm)	4.24575
Gap thickness (μm)	82.55
Cladding thickness (μm)	571.5

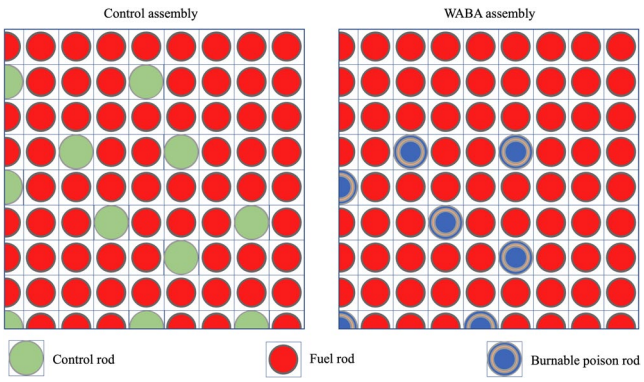

Fig. 2 (Color online) 1/4 Configuration of control and WABA assembly

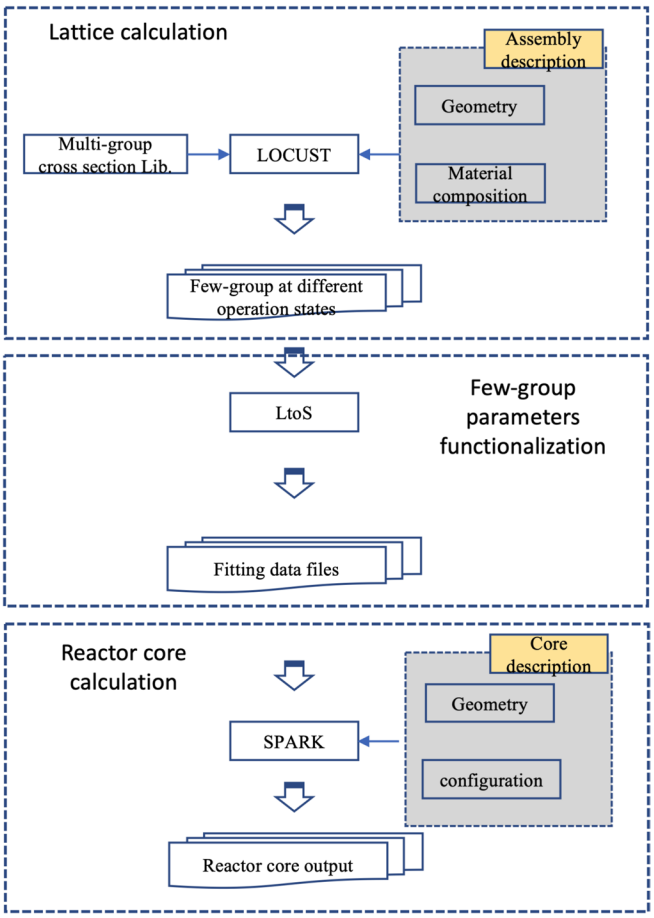

Fig. 3 Bamboo-C code calculation flowchart

where Bu_m and Bu_n are the two burn points in the reference burnup calculation. Bu_x and Bu_y are branch burnup calculations and c_m, c_n, c_x, and c_y are interpolation coefficients.

The SPARK code employs a nodal expansion method based on nonlinear iterations to solve the three-dimensional (3D) neutron diffusion equation. In the transient calculations, the time derivative term in the diffusion equation is treated using the theta method. Thermal–hydraulic feedback utilizes parallel multichannel models for steady-state and transient calculations. Compared to time-consuming computational fluid dynamics (CFD) or subchannel models, multichannel models ignore the cross-flow between fuel rods, which can have a large impact on heat transfer. However, this impact can be corrected using the equivalent convection heat transfer coefficient. In the parallel multichannel thermal–hydraulic calculation, each assembly consisted of four meshes in the radial direction, and each mesh was treated as an independent channel. The flow distributions in these channels were determined using equal pressure drops. The macro-/microburnup method was adopted to calculate the reactor core burnup distribution, evolution of heavy metal nuclides, and changes in the fission product density. More detailed information can be obtained in reference [41, 42].

2.4 Homogenization and functionalization of few-group parameters

The few-group parameters of three types of assembly, including control, WABA, and reflector assemblies, were generated using the LOCUST code. Two energy groups with demarcation energies of 0.625 eV were used. When homogenizing the fuel assemblies at LOCUST, geometrically fine modeling of the fuel assembly was performed, and reflective boundary conditions were applied. The fuel rod was divided into nine flat source regions with radii ranging from 0.1 to 0.42 cm. The gap and cladding were divided into one flat source region. The water region outside the cladding was divided into five flat source regions with radii of 0.495, 0.50, 0.53, 0.56, and 0.60 cm. For the WABA rod, the absorber region was divided into four flat source regions, whereas the other water and cladding regions were divided into one flat source region.

The leakage spectrum in the surrounding water reflector plays an important role in the accuracy of few-group parameters. According to the type of adjacent assembly, the few-group homogenized parameters of the four types of water reflectors were generated using three homogenization models, as shown in Fig. 4. The right boundary condition of the water reflector was a vacuum in all the models, and the other boundary conditions were reflective. The arrangements of the four types of homogenized water reflectors in the 1/4 reactor core are shown in Fig. 4. Notably, the assembly discontinuity factor was adopted in the calculation.

The thermal–hydraulic feedback must be considered in the following calculations. The few-group parameters for the discrete-state parameters were calculated using LOCUST and functionalized by LtoS code. Based on the characteristics of ACPR50S, the control rod fraction (CR), coolant density (DC), fuel temperature (TF), and coolant temperature (TC) were employed for functionalization. CR has only two states in 2D lattice calculation: fully withdrawn and fully inserted. Ten points were used for the DC: 0.8158 g/cm^3, 0.8015 g/cm^3, 0.7861 g/cm^3, 0.7697 g/cm^3, 0.7521 g/cm^3, 0.7329 g/cm^3, 0.6883 g/cm^3, 0.6612 g/cm^3, 0.6283 g/cm^3. Six state points were used for TF: 800 K, 900 K, 1000 K, 1100 K, 1200 K, and 1300 K. TC contained 10 state points: 520 K, 530 K, 540 K, 550 K, 560 K, 570 K, 580 K, 590 K, 600 K, and 610 K. In the LOCUST calculation, the reference states of TF, TC, and DC are 1000 K, 570 K, and 0.7329 g/cm^3, respectively. The burnup state points consisted of four segments from 0 to 30 GWd/tU. Each segment has an equal burnup step: 4.8 MWt/tU for 0–120 MWd/tU,

120 MWd/tU for 120–2520 MWd/tU, and 600 MWd/tU for 2520–30000 MWd/tU.

2.5 Reactor core calculation

In the reactor core neutronic calculation, each homogenized assembly region was radially divided into four meshes. The active core with a height of 250 cm was divided into 25 layers with thicknesses of 10 cm. The upper and lower reflectors, each 10 cm in thickness, were equally divided into two layers. The boundary conditions were set to a vacuum. The mesh used in the thermal–hydraulic calculation was the same as that used in the neutronic calculation. The total thermal power of the core was 300 MW with an average power of 8.1081 MW per fuel assembly, and the coolant inlet temperature was 286 °C with a mass flow rate of 82.12102 kg/s for each assembly.

As shown in Fig. 1, the reactor had four control rod banks: A, B, C, and D. When fully inserted, the bottom of the control rod remained at the bottom of the active core. Each control rod moving step was 1 cm; thus, step 0 corresponded to full insertion, and step 260 corresponded to full withdrawal. In burnup calculations, the control rods must be adjusted to keep the reactor core critical. Thus, the bottom of the control rod may remain inside a node, and strong neutron absorption causes a distorted flux distribution at this node. Traditional volume weighting methods cannot ensure the conservation of reaction rates before and after the homogenization of this node when the control rod is partly inserted, resulting in a large error, that is, the control rod cusping effect.

In the SPARK code, a 1D transverse integration equation was solved using the fine-mesh finite difference method for an axially adjacent three-node model, as shown in Fig. 5. Subsequently, a fine-mesh neutron flux was used to correct the control rod cusping effect. The axial boundary condition of the neutron current was determined using the 3D nodal method, and the radial boundary was represented by the transverse leakage. Therefore, the fine-mesh fluxes in the three local nodes were calculated, and the homogenized few-group parameters of a node with a partially inserted control rod can be obtained by flux volume weighting.

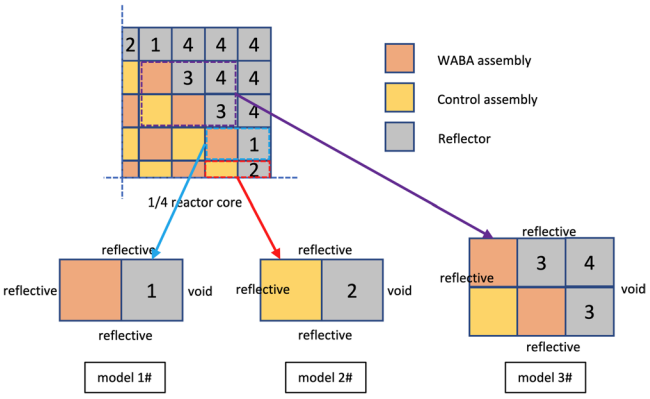

Fig. 4 (Color online) Reflector homogenization model

3 Steady-state analysis

Similar to the homogenization method, reactor core configuration, and core calculation methods mentioned above, a steady-state analysis of ACPR50S, including burnup calculations, reactivity coefficients, power/temperature distributions, and control rod worth, is performed for different ATFs: BeO + UO_2− SiC, BeO + UO_2− FeCrAl, U_3Si_2 − SiC, and U_3Si_2− FeCrAl.

3.1 Burnup calculation

Four different B-10 enrichments of 0%, 5%, 10%, and 20% were used in ACPR50S. The k_{eff} variation with operation time is shown in Fig. 6. The figure shows that different ATF cases exhibit similar trends. B-10 enrichments of both 20% and 10% have a large reactivity penalty at the end of life (EOL), and 5% B-10 enrichment can effectively reduce the initial residual reactivity without significantly decreasing the operational lifetime. A comparison of different ATF cases at 5% B-10 enrichment is shown in Fig. 7. The residual reactivity of BeO + UO_2 was higher than that of U_3Si_2 for the same cladding material and B_4C. This is because the moderating ability of BeO–UO_2 is better than that of U_3Si_2. The core with BeO + UO_2 has a shorter operation lifetime of approximately 50 days compared with the core with U_3Si_2. In addition, FeCrAl cladding has a larger neutron absorption than SiC, and using SiC can increase the operation time by 200 days for the same fuel. As depicted in Fig. 7, the cladding type had a greater impact on the lifetime than the fuel type. The burnup comparison shows that the BeO + UO_2 fuel and SiC cladding are superior to the other types.

3.2 Reactivity coefficient

The reactivity coefficient is a key safety parameter. In addition to depletion and fission product accumulation, the fuel temperature, moderator temperature, and void fraction also affect the reactivity. In this section, the fuel temperature, coolant temperature, void reactivity, and power coefficients are calculated.

During normal operation, the fuel temperature generally remains in the range of 900–1200 K. In the fuel temperature coefficient calculation, fuel temperature points were set at intervals of 100 K, and the coolant temperature was maintained at 600 K. The fuel temperature coefficients of cores

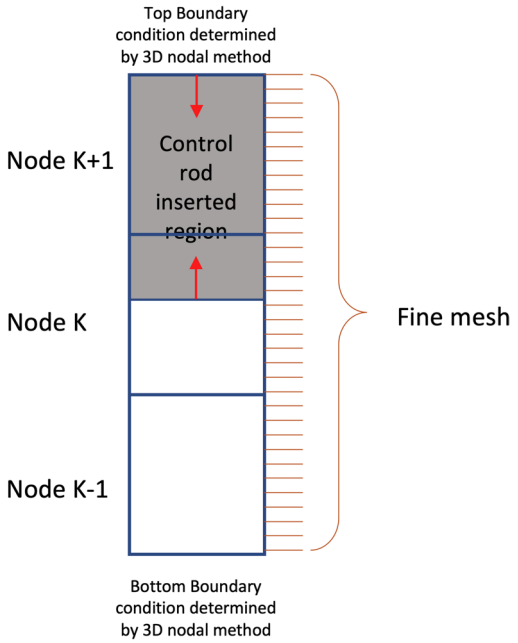

Fig. 5 (Color online) Three-node model in SPARK for correction of control rod cusping effect

with different ATFs are listed in Table 2. The table shows that the fuel temperature coefficients are −2.74 pcm/K, −2.54 pcm/K, −2.348 pcm/K, and −2.161 pcm/K for the four ATFs, which are all negative. The fuel temperature coefficient of BeO + UO_2− SiC is more negative than those of the others, whereas U_3Si_2− FeCrAl has the smallest negative coefficient. As mentioned above, BeO + UO_2 has a stronger moderation ability than the other fuel types. More fast neutrons entered the resonance energy region, and the fuel Doppler effect was more pronounced, resulting in a more negative fuel temperature coefficient. Fe nuclides in FeCrAl cladding can absorb a few resonant neutrons, thereby weakening the Doppler effect. From the viewpoint of the fuel temperature coefficient, ACPR50S fueled with BeO + UO_2 − SiC performed better than the other cases.

Water in ACPR50S acts as both a coolant and moderator. The change in the water temperature influences its density, which in turn affects its moderation ability and neutron absorption. During normal operation, the water temperature changes in the range of 520–610 K. An interval of 10 K was employed for the coolant temperature reactivity calculation, and the density and temperature changed synchronously. Figure 8 shows the change in k_{eff} with the coolant

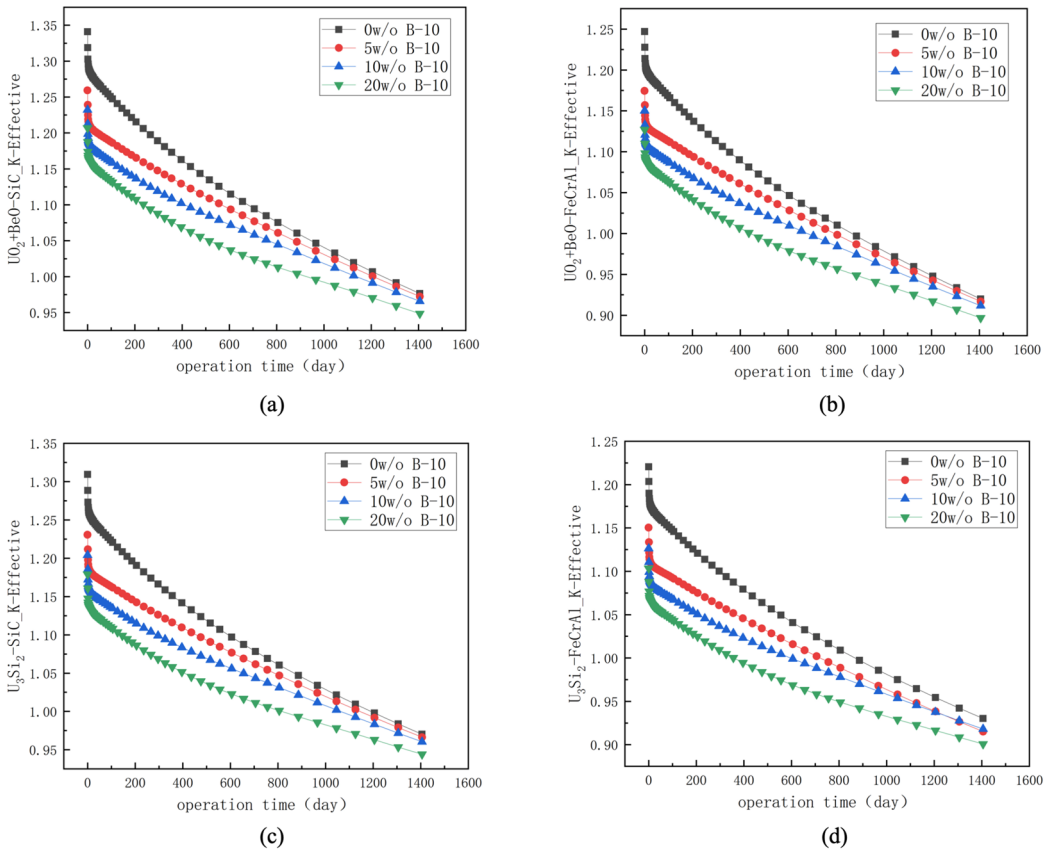

Fig. 6 (Color online) k_{eff} variation with operation time for ACPR50S with different ATFs and different B-10 enrichments. (**a**) BeO + UO_2− SiC (**b**) BeO + UO_2− FeCrAl (**c**) U_3Si_2 − SiC (**d**) U_3Si_2 − FeCrAl

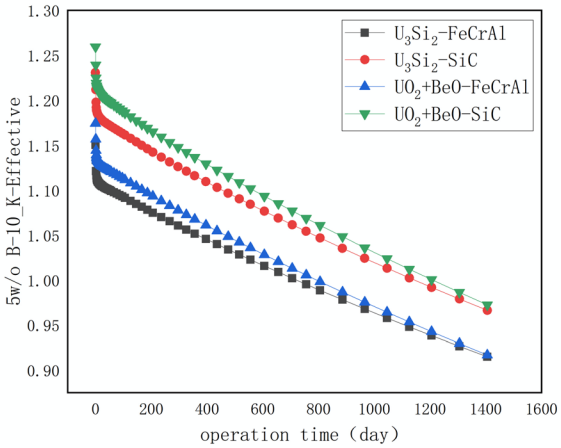

Fig. 7 (Color online) Comparison between different ATF cases at 5% B-10 enrichment

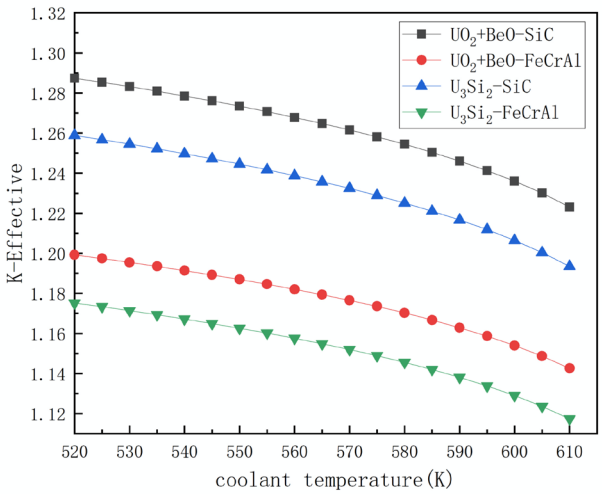

Fig. 8 (Color online) k_{eff} Changes with coolant temperature

temperature. The reactivity decreases with an increase in coolant temperature, which means that the coolant temperature coefficient is negative. Table 2 lists the reactivity variation when the coolant temperature changes between 520 and 610 K and the coolant temperature coefficient. Notably, ACPR50S does not contain soluble boron; thus, the negative value of the coolant temperature coefficient is relatively large because soluble boron has a positive effect on the coolant temperature coefficient. Fuels with the same cladding had similar reactivity coefficients, and the SiC-case is more negative than the FeCrAl-case. FeCrAl cladding has stronger thermal neutron absorption than SiC, which has a positive effect on the coolant temperature coefficient.

The change in the void fraction in the coolant plays an important role in reactivity, especially in loss-of-coolant accidents. An increase in the void fraction in the coolant reduces the moderation ability. Therefore, the neutron spectrum hardens, resulting in an increased neutron leakage and decreased reactivity. The void reactivity coefficient was calculated by setting the void fractions to 0% and 100%. The fuel and coolant temperatures were 900 K and 600 K, respectively. The results are listed in Table 2. The table shows that the void reactivity coefficients are all negative for ACPR50S in the four ATF cases. Similarly, the absence of soluble boron in the coolant led to a significantly negative void reactivity coefficient. Compared to SiC cladding, FeCrAl had stronger neutron absorption, and the void coefficient of SiC-based ATFs was more negative. The power coefficient was also calculated for these four ATFs, which was a comprehensive quantity that included the fuel temperature, coolant temperature, and void effects. The results are listed in Table 2. The table shows that the four cases have negative power coefficients, which meet the core-design safety criteria. Due to the combined influence of the strong moderation ability of BeO + UO_2 and small neutron absorption of SiC, the power coefficient −8.76 pcm/% FP of BeO + UO_2− SiC was more negative compared with the other three cases.

In summary, the reactivity coefficients ACPR50S of the four ATFs were all negative. ATFs with the same cladding had similar coolant temperature, void reactivity, and power coefficients because the neutron absorption of the cladding played a major role. For the temperature coefficient, the strong moderating ability of BeO + UO_2 had a negative effect; however, the neutron absorption of FeCrAl cladding caused a positive effect. Thus, the fuel temperature coefficient of BeO + UO_2− SiC fuel was 2.74 pcm/K more

Table 2 Reactivity coefficient for different cores

ATF type	Fuel temperature coefficient (pcm/K)	Coolant-temperature coefficient (pcm/K)	Void coefficient (pcm/%)	Power coefficient (pcm/%FP)
BeO + UO_2 − SiC	−2.74	−71.4	−479.4	−8.76
BeO + UO_2 − FeCrAl	−2.54	−62.9	−433.9	−7.78
U_3Si_2 − SiC	−2.34	−72.7	−483.0	−8.25
U_3Si_2 − FeCrAl	−2.16	−64.2	−440.3	−7.57

negative than the other three cases. Because of the absence of soluble boron in the coolant, the coolant temperature and void reactivity coefficients were significantly more negative than those of general PWRs.

3.3 Power and temperature distribution

The assembly normalized power, fuel temperature, and coolant temperature distributions of ACPR50S for the four ATFs were calculated, as shown in Fig. 9, where A, B, C, and D represent the $BeO + UO_2$– SiC, $BeO + UO_2$– FeCrAl, U_3Si_2– SiC, and U_3Si_2– FeCrAl cases, respectively. In the calculation, the nominal power of the 300 MWth and coupling thermal–hydraulic calculations were performed, and all control rods remained outside the reactor core.

As shown in Fig. 9, the power peak factors of $BeO + UO_2$ – SiC and $BeO + UO_2$– FeCrAl were 1.63 and 1.65, respectively, which were marginally larger than those of the other two cases. This is because $BeO + UO_2$ had a strong moderating ability and SiC-based ATF had a low fuel temperature owing to the high thermal conductivity of SiC[43]. The fuel temperature distributions of the four cases were similar, and the gradient of the cases fueled by $BeO + UO_2$ was larger than that of U_3Si_2. The maximum fuel temperature of the core fueled by $BeO + UO_2$ was approximately 604 °C. However, the maximum fuel temperature of the core fueled by U_3Si_2 was approximately 595 °C. The coolant temperature distributions of the four ATF cases were nearly identical because all heat generated by the fission reaction was transferred to the coolant at the steady state. The maximum coolant temperature was approximately 327 °C, and the difference between the maximum and minimum values of the entire core did not exceed 20 °C.

At a nominal power of 300 MWth, comparison analyses were performed for ACPR50S with the four ATFs, including the normalized power distribution, fuel temperature distribution, and moderator temperature distribution. The U_3Si_2 fuel core had a better power-flattening effect than $BeO + UO_2$, and the overall fuel temperature change was smaller. Moreover, the coolant temperature distributions differed marginally among all ATF cases. Although the moderating abilities of UO_2– BeO and U_3Si_2 and the neutron absorption of SiC and FeCrAl differed, these differences had a small impact on the power and temperature distributions.

3.4 Reactivity worth

ACPR50S adopts burnable poison and control rods to adjust the reactivity. Twenty-one burnable poison and 16 control assemblies were configured in the reactor core. Both the burnable poison and control rod reactivity worth were calculated, as shown in Table 3 and Fig. 10. Burnable poison reactivity worth is defined as the reactivity difference between loading pure fuel without burnable poison (0% B-10 enrichment) and loading burnable poison (5% B-10 enrichment). ACPR50S loaded with $BeO + UO_2 -$ SiC had the largest burnable poison reactivity, worth 8153 pcm, because BeO had a better moderating ability than U_3Si_2. For the same fuel type, FeCrAl cladding had a larger absorption cross section than SiC, which resulted in a reactivity penalty of approximately 800 pcm.

ACPR50S employs four groups of control rods: A, B, C, and D. The differential and total reactivity worths of the four control rod groups were calculated. In the calculations for a control rod group, the other control rod groups remained outside the reactor core, and a B-10 enrichment of 5% was employed. Furthermore, the correction method for the control rod cusping effect was employed in the differential worth calculation using the Bamboo-C code. $BeO + UO_2 -$ SiC had the maximum total control rod reactivity of 29638 pcm among all ATF cases, and $U_3Si_2 -$ FeCrAl had the minimum (25430 pcm). When all poisons were inserted into the reactor, a shutdown margin of 1300 pcm of the design criteria was reached. Figure 10 shows that control rod group B had the largest differential worth, and A had the smallest because control rod A stays in the outer region of the reactor core, whereas B stays in the inner region. For all control rod groups, the differential worth appeared similar between different ATFs, and the maximum difference did not exceed 10 pcm/step.

ACPR50S did not contain soluble boron; thus, criticality is maintained by adjusting the control rod position, and the order of adjustment was B–A–C–D. During the operation, the critical positions of the control rod were calculated for the four ATFs, as shown in Fig. 10, where the fully inserted and withdrawn control rods corresponded to steps 0 and 260, respectively. Because of the difference in the initial residual reactivity, the critical position of control rod B in step 30 was reached for the $BeO + UO_2 -$ SiC core, and the $U_3Si_2 -$ FeCrAl core had the highest critical position in step 67. The critical positions of the control rod were different for ACPR50S fueled by different ATFs. Comparing all cases, the control rods of the $U_3Si_2 -$ FeCrAl core were the first to be fully withdrawn, and those of $BeO + UO_2 -$ SiC were the last. Control rod groups B, A, C, and D of the $U_3Si_2 -$ FeCrAl core were fully withdrawn on days 166, 186, 516, and 806, respectively. However, those for the $BeO + UO_2 -$ SiC core were observed on days 556, 606, 1046, and 1406.

4 Transient analysis

Transient characteristic analysis is an important aspects of safety design. In this section, the transients of the control rod ejection accident for two control rods with the

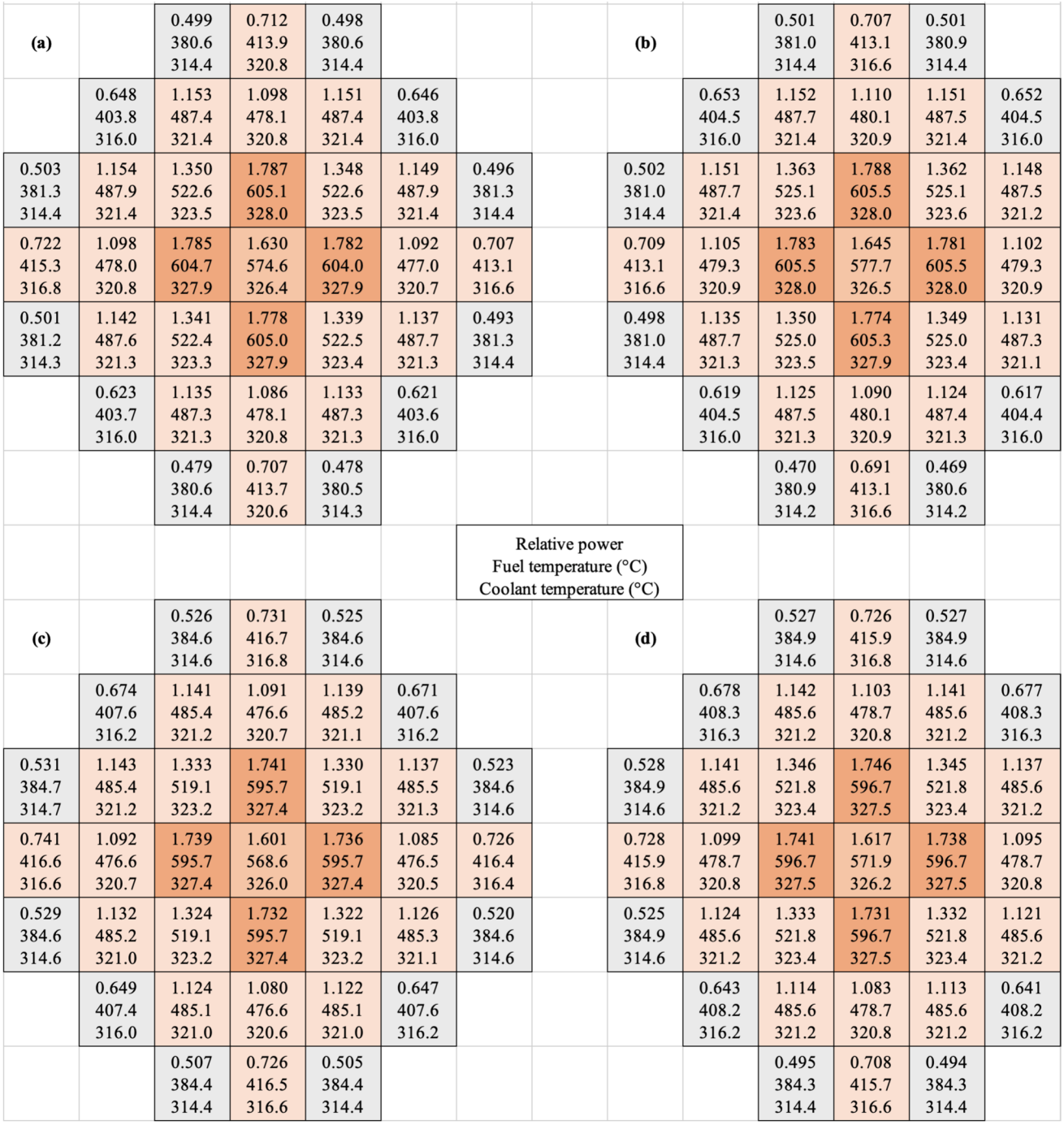

Fig. 9 (Color online) Normalized power and temperature distribution ACPR50S for four ATF types, **a** BeO + UO_2 − SiC **b** BeO + UO_2 − FeCrAl **c** U_3Si_2 − SiC **d** U_3Si_2 − FeCrAl

maximum and minimum reactivity worth are analyzed. In the transient state, control rod A was ejected from steps 0 to 100, control rod B was ejected from step 100 to fully withdrawn, and each step was 1 cm.

In the calculation, the control rod ejection was completed in 0.1 s, a time step of 0.01 s was employed, and the entire simulation continued for 10 s. At the beginning of the transient, the reactor core maintained criticality by adjusting the nu-fission cross section because the critical control rod position was different for different ATFs, and the reactor core remained in a hot and full-power state. The reactivity changes caused by the control rod ejection are illustrated in Fig. 11. At time 0 s, the positive reactivity increased quickly owing to the control rod ejection. The

Table 3 Reactivity worth for four types of ATF

ATF type	Burnable poison worth (pcm)	Control rod total worth (pcm)
$BeO + UO_2 - SiC$	8153.0	29,638
$BeO + UO_2 - FeCrAl$	7240.7	26,114
$U_3Si_2 - SiC$	7873.7	28,732
$U_3Si_2 - FeCrAl$	7012.9	25,430

reactor power and core temperature increased simultaneously. The negative reactivity feedback then restrained the increase in reactivity, and it reached a maximum value at approximately 0.4 s. Furthermore, the negative reactivity feedback started to dominate, and the reactivity decreased smoothly. For different ATF types, the reactivity changed similarly, and the $U_3Si_2 - SiC$ core exhibited the largest reactivity insertion. The maximum difference in the reactivity insertion between different ATF cases was approximately 0.09 $ for control rod A and 0.02 $ for control rod B.

The core power response during the transient is shown in Fig. 11. Control rod ejection introduced positive reactivity, causing a rapid increase in the reactor core power. However, the negative feedback of the fuel and coolant temperature reduced the core power, eventually stabilizing it at a new level. In the transient of the control rod A ejection, the core power of the $U_3Si_2 - SiC$ core changed the most and reached the maximum relative power of 1.85 at time 0.11 s. However, the $BeO + UO_2 - FeCrAl$ core with the slowest increase reached a maximum relative power of 1.60 at time 0.19 s. The power changes were similar for the control rod B ejection case. The $U_3Si_2 - SiC$ core reached a maximum relative power of 2.5 at time 0.08 s, and the $BeO + UO_2 - FeCrAl$ core reached a maximum relative power of 2.29 at time 0.08 s because control rod B had a larger reactivity worth than control rod A. The power response of the core fueled by $BeO + UO_2$ changed more gradually than that of the other ATFs during the positive reactivity insertion transient owing to the more negative fuel and coolant temperature coefficients.

The changes in the fuel and coolant temperatures during the transient were also calculated, as illustrated in Fig. 11. The fuel temperature increased quickly at the beginning of the transient, along with an increase in reactor power, and then became steady. Similar to the core power response in the transient ejection of both control rods A and B, the fuel temperature of the $U_3Si_2 - SiC$ core reached the highest values of 516 °C and 560 °C, respectively, when reaching stability. Conversely, the $BeO + UO_2 - FeCrAl$ core exhibited the lowest fuel temperatures of 511 °C and 552 °C, respectively, after reaching stability. The coolant temperature and density changed similarly with the fuel temperature in the transient, and the maximum difference in the average coolant temperature between the cores fueled by different ATFs did not exceed 2 °C. Overall, during the same control rod ejection, the changes in the fuel and coolant temperatures and density appeared to be minimal, with only a maximum difference of 10 °C for the fuel temperature and 2 °C for the coolant temperature. The transient responses mainly depended on the neutronic and thermal–hydraulic characteristics of the ATFs. Although differences exist in the moderation ability of UO_2-BeO and U_3Si_2 and neutron absorption of SiC and FeCrAl, these differences have a small impact on the change in reactivity insertion and relative core power during the transient state.

5 Conclusion

This study focused on the coupling neutronics and thermal–hydraulic analysis of a SPWR, ACPR50S, for different ATFs including $BeO + UO_2 - SiC$, $BeO + UO_2 - FeCrAl$, $U_3Si_2 - SiC$, and $U_3Si_2 - FeCrAl$, using the Bamboo-C deterministic code developed by the NECP laboratory.

A steady-state analysis, including burnup calculations, reactivity coefficients, power and temperature distributions, and control rod reactivity worth, was performed. A 5% B-10 enrichment in the WABA assembly effectively reduced the initial reactivity and EOL reactivity penalty. The reactivity coefficients ACPR50S of the four ATFs were all negative. Owing to the good moderation ability of $BeO + UO_2$ and the small neutron absorption of SiC, the $BeO + UO_2 - SiC$ core has better burnup characteristics and a more negative fuel temperature reactivity coefficient and power coefficient compared to other ATFs. The $BeO + UO_2 - SiC$ and $U_3Si_2 - SiC$ cores had coolant temperature and void reactivity coefficients similar to those of the other cases because the neutron absorption of FeCrAl had a positive effect. The U_3Si_2 fuel core had a better power-flattening effect than $BeO + UO_2$, and the fuel and coolant temperatures differed little among all ATF cases. The differential worth of each control rod group appeared similar between different ATFs, and the maximum difference did not exceed 10 pcm/step.

Two transient states were also calculated, including control rod ejection accidents with the maximum and minimum reactivity worth. The maximum difference in the reactivity insertion between different ATF cases was approximately 0.09 $ for control rod A and 0.02 $ for

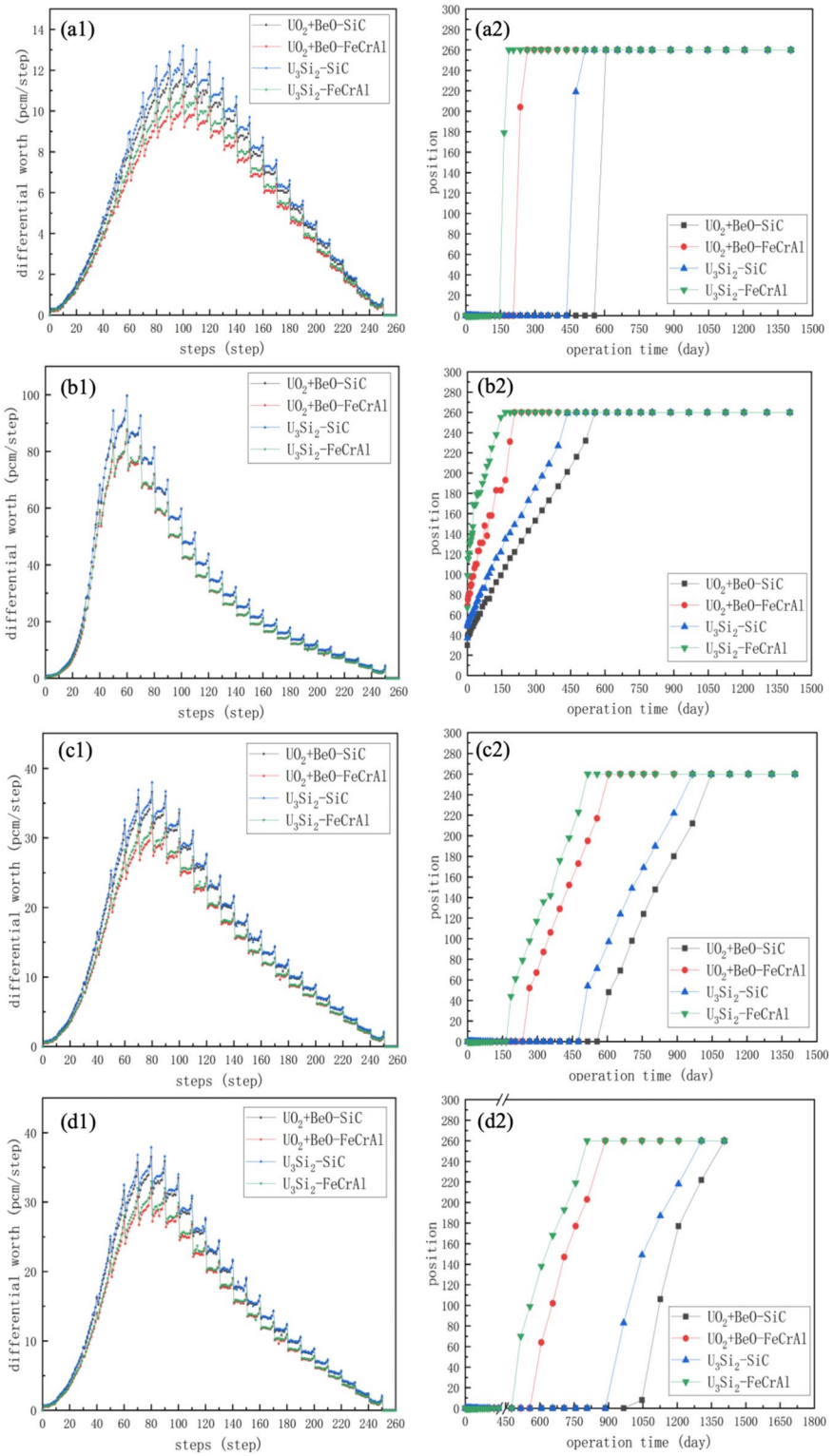

Fig. 10 (Color online) Differential control worth and critical position for four types of ATF, where **a1**, **b1**, **c1**, **d1**, respectively, refer to differential control worth of control rod groups A, B, C, D, and **a2**, **b2**, **c2**, **d2** are, respectively, critical position of control rod groups A, B, C, D

control rod B. The changes in the fuel temperature, coolant temperature, and coolant density in the transient of the same control rod ejection were similar. The maximum difference did not exceed 10° for the fuel temperature and 2° for the coolant temperature. Although differences exist in the moderating ability of UO_2-BeO and U_3Si_2 and the neutron absorption of SiC and FeCrAl, these differences had a small impact on the change in reactivity insertion and relative core power during the transient state.

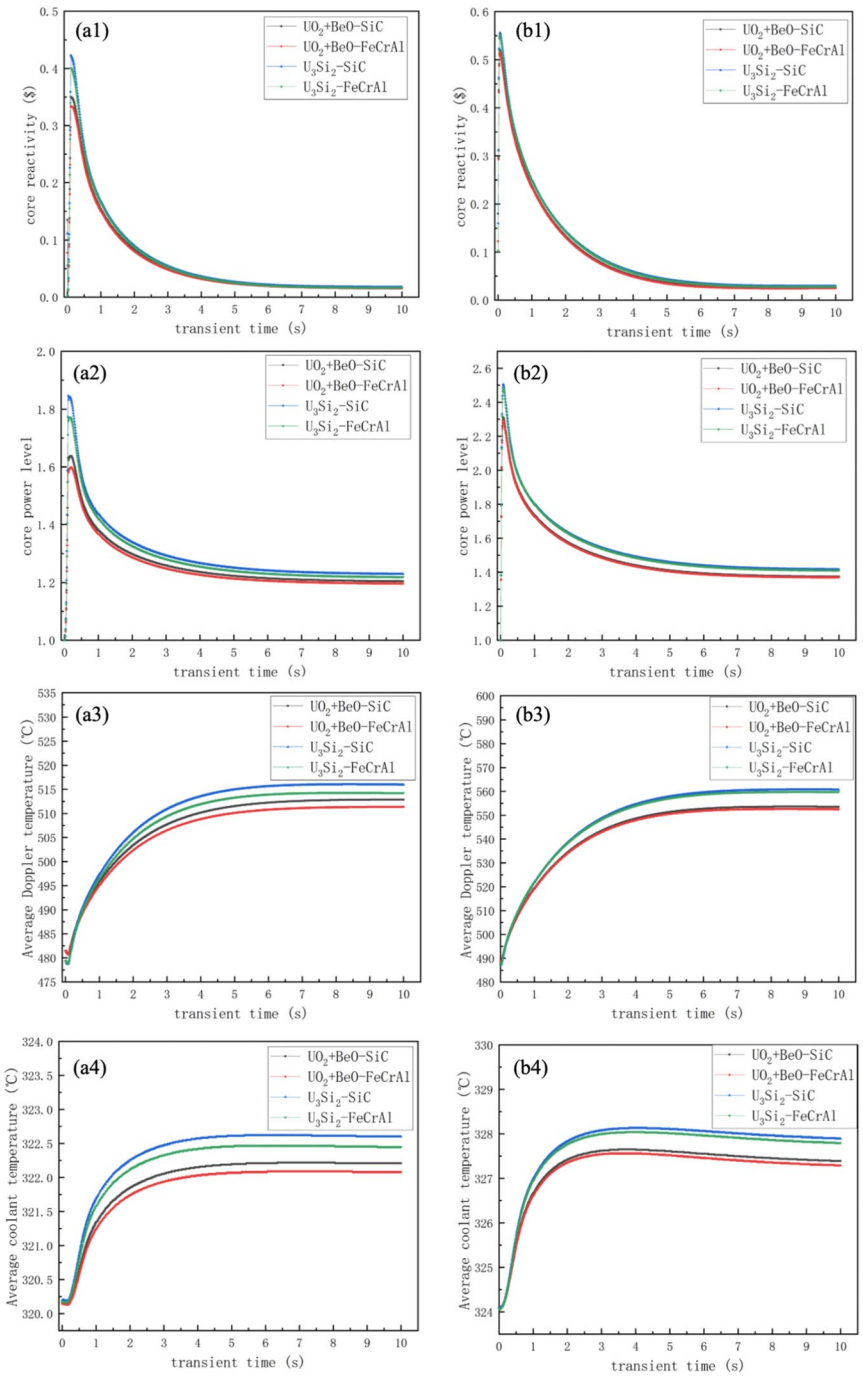

Fig. 11 (Color online) Transient response for control rod ejection, where **a1**, **a2**, **a3**, **a4** are, respectively, core reactivity, core power, fuel temperature, coolant temperature for control rod group A, and **b1**, **b2**, **b3**, **b4** are, respectively, core reactivity, core power, fuel temperature, coolant temperature for control rod group B

Author Contributions All authors contributed to the study conception and design. Material preparation, data collection and analysis were performed by Kun Zhuang, Ying-Zhen Wang, Lina Deng, Yong-Zhan Wang, Wen Shang and Si-Peng Wang. The first draft of the manuscript was written by Kun Zhuang and Ying-Zhen Wang, and all authors commented on previous versions of the manuscript. All authors read and approved the final manuscript.

Data Availability The data that support the findings of this study are openly available in Science Data Bank at https://cstr.cn/31253.11.sciencedb.j00186.00187 and https://doi.org/10.57760/sciencedb.j00186.00187.

Declarations

Conflict of interest The authors declare that they have no conflict of interest.

References

1. National Education Association, *Small Modular Reactors: Challenges and Opportunities* (OECD Publishing, Paris, 2021)

2. Y. Xu, S. Hu, F. Li et al., High temperature reactor development in China. Prog. Nucl. Energy **47**, 260–270 (2005). https://doi.org/10.1016/j.pnucene.2005.05.026
3. H.B. Magana, D.F. Delmastrob, M. Markiewiczb et al., CAREM prototype construction and licensing status. *Paper Presented at International Conference on Opportunities and Challenges for Water Cooled Reactors in the 21*. century, Vienna, Austria, 27–30 Oct (2009)
4. International Atomic Energy Agency, *Deployment Indicators for Small Modular Reactors* (International Atomic Energy Agency, Vienna, 2018)
5. J.A. Halfinger, M.D. Haggerty, The B &W mPower scalable, practical nuclear reactor design. Nucl. Technol. **178**, 164–169 (2012). https://doi.org/10.13182/NT11-65
6. D.L. Zverev, A.N. Pakhomov, V.I. Polunichev et al., RITM-200: new-generation reactor for a new nuclear icebreaker. Atom. Energy+ **113**, 404–409 (2013). https://doi.org/10.1007/s10512-013-9653-7
7. C.D. Bell, Approach to UK SMR component design. *Paper Presented at International Conference on Nuclear Engineering*, London, England, 22–26 July (2018)
8. K.K. Kim, W. Lee, S. Choi et al., SMART: the first licensed advanced integral reactor. J. Energy Power Eng. **8**, 94–102 (2014). https://doi.org/10.17265/1934-8975/2014.01.011
9. X. Li, L. Li, L. Peng et al., Conceptual core design of HAPPY200 reactor. *Paper Presented at International Conference on Nuclear Engineering*, London, England, 22–26 July (2018)
10. D. Zhu, Q. Xiang, M. Zhang et al., Evaluation of in-vessel corium retention margin for small modular reactor ACP100. Ann. Nucl. Energy **94**, 684–690 (2016). https://doi.org/10.1016/j.anucene.2016.04.015
11. J. Huang, N. Li, Y. Zhang et al., The safety analysis of a small pressurized water reactor utilizing fully ceramic microencapsulated fuel. Nucl. Eng. Des. **320**, 250–257 (2017). https://doi.org/10.1016/j.nucengdes.2017.05.022
12. J. Huang, N. Li, Y. Zhang et al., The excess reactivity management in small pressurized water reactor utilizing fully ceramic microencapsulated fuel. Prog. Nucl. Energy **101**, 251–259 (2017). https://doi.org/10.1016/j.pnucene.2017.08.005
13. F.C. McGinty, Nuclear power plants and maintainability. Hum. Factors **7**, 355–361 (1965). https://doi.org/10.1177/001872086500700406
14. J. Buongiorno, J. Jurewicz, M. Golay et al., The offshore floating nuclear plant concept. Nucl. Technol. **194**, 1–14 (2016). https://doi.org/10.13182/NT15-49
15. D.T. Ingersoll, Z.J. Houghton, R. Bromm et al., NuScale small modular reactor for co-generation of electricity and water. Desalination **340**, 84–93 (2014). https://doi.org/10.1016/j.desal.2014.02.023
16. S. Beliavskii, M. Balachkov, V. Danilenko et al., Fuel lifetime extension for the KLT-40S small modular reactor by means of thorium-uranium fuel cycle. Ann. Nucl. Energy **192**, 109982 (2023). https://doi.org/10.1016/j.anucene.2023.109982
17. S. Beliavskii, N. Anikin, S. Alhassan et al., Effect of fuel nuclide composition on the fuel lifetime of the RITM-200 reactor unit. Ann. Nucl. Energy **173**, 109105 (2022). https://doi.org/10.1016/j.anucene.2022.109105
18. A.V. Zrodnikov, G.I. Toshinsky, O.G. Komlev et al., SVBR-100 module-type fast reactor of the IV generation for regional power industry. J. Nucl. Mater. **415**, 237–244 (2011). https://doi.org/10.1016/j.jnucmat.2011.04.038
19. Z. Chireuding, M. Yi, T. Akira et al., Integral PWR-type small modular reactor developmental status, design characteristics and passive features: a review. Energies **13**, 2898 (2020). https://doi.org/10.3390/en13112898
20. R. Mazzi, CAREM: An Innovative-Integrated PWR. *Paper Presented at the SMiRT 18*, Beijing, China, 7–12 August (2005)
21. K. Hibi, H. Ono, T. Kanagawa, Integrated modular water reactor (IMR) design. Nucl. Eng. Des. **230**, 253–266 (2004). https://doi.org/10.1016/j.nucengdes.2003.11.025
22. Z. Liu, B. Yang, L. Tian, F. Zhang, Development and outlook of advanced nuclear energy technology. Energy Strategy Rev. **34**, 100630 (2021). https://doi.org/10.1016/j.esr.2021.100630
23. S.J. Zinkle, K.A. Terrani, J.C. Gehin et al., Accident tolerant fuels for LWRs: a perspective. J. Nucl. Mater. **448**, 374–379 (2014). https://doi.org/10.1016/j.jnucmat.2013.12.005
24. B. Lan, X. Pan, S. Yu et al., Control rod ejection accident simulation and sensitivity analysis of large advanced pressurized water reactor. Nucl. Technol. **46**, 020601 (2023). https://doi.org/10.11889/j.0253-3219.2023.hjs.46.020601. (**in Chinese**)
25. H. Wang, D. Yang, H. Cheng et al., Chemical interaction layer between uranium oxide fuel pellet and zirconium alloy cladding in pressurized water reactor. Nucl. Technol. **46**, 090602 (2023). https://doi.org/10.11889/j.0253-3219.2023.hjs.46.090602. (**in Chinese**)
26. N.R. Brown, A.T. Nelson, K.A. Terrani, *Comprehensive Nuclear Materials*, 2nd edn. (Elsevier, Amsterdam, 2020), pp.684–706
27. N.R. Brown, H. Ludewig, A. Aronson et al., Neutronic evaluation of a PWR with fully ceramic microencapsulated fuel. Part I: Lattice benchmarking, cycle length, and reactivity coefficients. Ann. Nucl. Energy **62**, 538–547 (2013). https://doi.org/10.1016/j.anucene.2013.05.025
28. J. Chun, S. Lim, B. Chung et al., Safety evaluation of accident-tolerant FCM fueled core with SiC-coated zircalloy cladding for design-basis-accidents and beyond DBAs. Nucl. Eng. Des. **289**, 287–295 (2015). https://doi.org/10.1016/j.nucengdes.2015.04.021
29. I. Younker, M. Fratoni, Neutronic evaluation of coating and cladding materials for accident tolerant fuels. Prog. Nucl. Energy **88**, 10–18 (2016). https://doi.org/10.1016/j.pnucene.2015.11.006
30. J. Wang, M. Mccabe, L. Wu et al., Accident tolerant clad material modeling by MELCOR: benchmark for SURRY short term station black out. Nucl. Eng. Des. **313**, 458–469 (2017). https://doi.org/10.1016/j.nucengdes.2017.01.002
31. Y.M. Mohsen, A.E. Abdel-Rahmana, A.A. Galahom, Integrated analysis of VVER-1000 fuel assembly fueled with accident tolerant fuel (ATF) materials. Ann. Nucl. Energy **159**, 108330 (2021). https://doi.org/10.1016/j.anucene.2021.108330
32. P. Sadiel, J. Francois, Neutronic analysis of the NuScale core using accident tolerant fuels with different coating materials. Nucl. Eng. Des. **377**, 111169 (2021). https://doi.org/10.1016/j.nucengdes.2021.111169
33. NRC, Review of accident tolerant fuel concepts with implications to severe accident progression and radiological releases. ERI/NRC 20-209(2020)
34. X. Dai, X. Cao, S. Yu et al., Conceptual core design of an innovative small PWR utilizing fully ceramic microencapsulated fuel. Prog. Nucl. Energy **75**, 63–71 (2014). https://doi.org/10.1016/j.pnucene.2014.04.010
35. Y. Liang, B. Lan, Q. Zhang et al., Neutronic analysis of silicon carbide cladding-ATF fuel combinations in small modular reactors. Ann. Nucl. Energy **73**, 109120 (2022). https://doi.org/10.1016/j.anucene.2022.109120
36. Q. Zhang, X. Wang, Y. Zhang et al., Neutronic analysis for potential Accident Tolerant Fuel UO_2-BeO in the light water reactor. Ann. Nucl. Energy **127**, 278–292 (2019). https://doi.org/10.1016/j.anucene.2018.12.014
37. Y. Liang, B. Lan, Q. Zhang et al., Neutronic analysis of silicon carbide Cladding-ATF fuel combinations in small modular reactors. Ann. Nucl. Energy **173**, 109120 (2022). https://doi.org/10.1016/j.anucene.2022.109120

38. X.L. Wu, W. Li, Y. Wang et al., Preliminary safety analysis of the PWR with accident-tolerant fuels during severe accident conditions. Ann. Nucl. Energy **80**, 1–13 (2015). https://doi.org/10.1016/j.anucene.2015.02.040
39. H. Yu, J. Cai, S. He et al., Analysis of neutron physics and thermal hydraulics for fuel assembly of small modular reactor loaded with ATFs. Ann. Nucl. Energy **152**, 107957 (2021). https://doi.org/10.1016/j.anucene.2020.107957
40. S. Chen, C. Yuan, Neutronic study of UO_2-BeO fuel with various claddings. Nucl. Mater. Energy **22**, 100728 (2020). https://doi.org/10.1016/j.nme.2020.100728
41. C. Wang, Y. Li, Y. Zheng et al., Code development and engineering validation of PWR fuel management software bamboo-C. Nuclear Power Eng. **42**, 15–22 (2021). https://doi.org/10.13832/j.jnpe.2021.05.0015. (**in Chinese**)
42. C. Wan, L. Guo, J. Bai, Method research and effect analysis of fuel-assembly bowing on neutron-physics simulations of HPR1000. Ann. Nucl. Energy **182**, 109616 (2023). https://doi.org/10.1016/j.anucene.2022.109616
43. B. Qiu, J. Wang, Y. Deng et al., A review on thermohydraulic and mechanical-physical properties of SiC, FeCrAl and Ti_3SiC_2 for ATF cladding. Nucl. Eng. Technol. **52**, 1–13 (2020). https://doi.org/10.1016/j.net.2019.07.030